Design, characterization and evaluation of Ce-modified cobalt catalysts supported on alpha alumina in the abatement of methane emissions from natural gas engines

Andoni Choya [a], Sylwia Gudyka [b], Beatriz de Rivas [a], Jose Ignacio Gutiérrez-Ortiz [a], Andrzej Kotarba [b], Rubén López-Fonseca [a],*

[a] Chemical Technologies for Environmental Sustainability Group, Department of Chemical Engineering, Faculty of Science and Technology, University of The Basque Country UPV/EHU, Barrio Sarriena s/n, Leioa, Bizkaia, E-48940, Spain
[b] Materials and Surface Chemistry Group, Faculty of Chemistry, Jagiellonian University, Gronostajowa 2, Krakow, P-30-387, Poland

ABSTRACT

This work deals with the optimisation of Ce-promoted Co_3O_4 catalysts supported on alpha alumina for the oxidation of traces amounts of methane. Ten Co-Ce samples were synthesised by incipient wetness coimpregnation with the aim of analysing the influence of the Ce/Co molar ratio and the Co_3O_4 loading on the physicochemical properties and resultant catalytic behaviour. Textural, structural, morphological and redox properties along with bulk/surface composition were thoroughly characterised. Lattice distortion provoked by insertion of controlled amounts of Ce increased the abundance of Co^{3+} and improved consequently the redox properties and the mobility of lattice oxygen species of the Co-Ce catalysts. Analysis of kinetic data in the $200-600$ °C temperature range evidenced that the optimal catalyst formulation was 10 %Co_3O_4wt. with a Ce/Co molar ratio of 0.05. In addition, this sample showed a reasonable stability with time on stream under cycled dry/humid conditions.

1. Introduction

Atmospheric pollution is a problem that becomes more and more notorious over time due to the population growth and the increase in the industrial activities such as transport that depend on fossil fuels for their operation. More specifically, the growing global concern about the harmful effects of automotive fuels, namely gasoline and diesel, on health and the environment together with less availability of oil for their production is forcing industrial companies to seek for alternative fuels with a minimal environmental impact [1]. In this context, natural gas as a vehicle fuel has gained notable interest as a possible candidate since engines powered by this fuel produce around 20–30 % less CO_2 and NO_x and virtually no particulate matter compared with traditional internal combustion engines [2]. However, their main disadvantage that limits their extensive application is the emission of unburned methane, which is a powerful greenhouse effect gas [3].

The most common approach to control methane emissions in natural gas engines is catalytic oxidation over noble metals, namely Pd and Pt, since they exhibit low-temperature efficiency and high intrinsic activity

[4–6]. In addition to the technical drawbacks related to their scarcity and the consequent high cost, these catalytic materials are also prone to deactivation by the presence of water in the feedstream [7,8]. For these reasons [9], and also in the light of the widely accepted current sustainable trend towards using less critical catalytic materials, such as noble metals, to yield comparable levels of efficiency, more attention has been paid to Co_3O_4-based catalysts as a versatile alternative due to the higher abundance, lower cost of cobalt and notable efficiency for CO [10,11], light hydrocarbons including methane [12–14], aromatic, oxygenated and chlorinated VOCs [15–17], and soot [18] oxidation.

The notable performance of this class of catalyst in these processes is controlled chiefly by reducibility and mobility of oxygen species. These properties in turn depend on the chemical affinity that exists between the active phase and the support, thus playing a direct role in metal distribution and finally in the catalytic activity, selectivity and stability. Hence, a strong interaction can result in the generation of poorly reducible species such as $CoAl_2O_4$, $CoSiO_3$ or Co-Mg-O mixed oxides when γ-Al_2O_3, SiO_2 or MgO are used as supports, respectively [19–21]. Therefore, the redox properties are adversely affected. Instead, the

* Corresponding author.
  E-mail address: ruben.lopez@ehu.es (R. López-Fonseca).

addition of a thin layer of a promoter oxide that acts as a physical barrier has been shown to prevent cobalt from partially forming these undesired cobalt oxides. For example, Choya et al. [22,23] have recently reported interesting results for Co_3O_4 catalysts supported on CeO_2-coated γ-alumina. This approach, however, involves greater complexity in the synthesis of the samples along with a higher total cost of the resulting catalysts. An alternative strategy could be the use of supports with a high chemical stability, namely alpha alumina, which could a priori maximise the amount of deposited cobalt as Co_3O_4. Although this alumina polymorph is characterised by a low surface area, which in turn may limit the dispersion and distribution of cobalt, $α-Al_2O_3$-supported cobalt catalysts have been successfully examined for a wide number of processes, such as Fischer-Tropsch process [24,25], total oxidation of propane [26], N_2O decomposition [27], ethanol steam reforming [28] and methane partial oxidation [29]. However, to the best of our knowledge the efficiency of this type of catalytic system ($Co_3O_4/α-Al_2O_3$) in the lean methane oxidation has not been investigated.

On the other hand, apart from minimising the percentage of Co ions strongly interacting with the carrier, the intrinsic oxidation activity of Co_3O_4 can be improved by inserting suitable metal dopants into the lattice of the cobalt spinel. In this sense, the addition of nickel has shown promising results since it may result in the formation of highly active $NiCo_2O_4$-like species [30]. Unfortunately, a fraction of added nickel can also interact with the alumina support, thus forming nickel aluminate with a low reducibility. Interestingly, a remarkable improvement in oxidation activity has also been found when incorporating controlled quantities of cerium since this promoter enhances oxygen mobility at low temperatures [31].

Therefore, the present work focuses on the analysis of Ce-modified cobalt catalysts supported on alpha alumina in the abatement of methane emissions from natural gas engines. The optimisation of this catalyst formulation will be approached by determining the most suitable Co_3O_4 loading, in the 2.5−20%wt.Co_3O_4 range, and Ce/Co molar ratio, between 0 and 0.2. Thus, a large number of samples were synthesised by incipient wetness coimpregnation and extensively characterised by BET measurements, EDXRF, XRD, Raman spectroscopy, XPS, STEM-HAADF coupled to EELS/EDX, HRTEM, and H_2-TPR, with the aim of defining rational relationships between the catalyst properties and the observed performance in the oxidation of trace amounts of methane.

2. Experimental

2.1. Synthesis of the Ce-promoted cobalt catalysts supported on α-Al_2O_3

Ten Ce-promoted Co_3O_4 catalysts supported over powdered $α-Al_2O_3$ with varying cobalt and cerium loadings were synthesised by incipient wetness coimpregnation. Thus, 2 g of the alumina support were impregnated with 2 mL of an aqueous solution with adjusted concentrations of cobalt (II) nitrate hexahydrate (Fluka)/cerium (III) nitrate hexahydrate (Merck) (3.8 and 0.2 M, respectively). The $α-Al_2O_3$ was prepared by calcination of boehmite (Versal) at 1300 °C for 6 h. Firstly, for a fixed Co_3O_4 loading (10 %wt.) the influence of the Ce/Co molar ratio between 0 and 0.2 was examined. Secondly, the effect of the Co_3O_4 content in the 2.5−20%wt. range was investigated while maintaining the Ce/Co molar ratio constant at 0.05. After the impregnation step, all precursors were dried at 110 °C for at least 16 h, and then calcined at 600 °C for 4 h in static air. The samples were denoted as xCo-yCe, where x and y stand for the Co_3O_4 and CeO_2 loadings, respectively.

2.2. Characterisation techniques and experimental reaction set-up

Textural properties, namely the specific surface area (BET method) and pore volume (BJH method), were evaluated by nitrogen physisorption at −196 °C in a Micromeritics TriStar II apparatus. All samples were pre-treated with flowing N_2 flow on a Micromeritics SmartPrep instrument at 300 °C for 10 h. The cobalt content of the catalysts was determined by energy-dispersive X-Ray fluorescence (EDXRF) using a Thermo Scientific ARLQUANT'X spectrometer operating with a Rh anode at 4−50 kV (with a 1 kV step) and a 1 mm size beam. A 3.5 mm Si (Li) drifted crystal detector with Peltier cooling was used. UniQuant software was employed for quantitation purposes.

X-Ray diffraction (XRD) analysis was carried out using a Bruker D8 ADVANCE instrument with $CuK_α$ radiation (λ = 1.5406 Å), in the 2θ range of 5−80° with a counting step of 0.2°. ICDD (International Centre for Diffraction Data) database cards were used for comparative purposes to identify the phases present in the samples. Additional diffraction patterns were taken on a X'PERT-PRO X-Ray diffractometer using Cu Kα radiation (λ = 1.5406 Å) and a Ni filter at 40 kV and 40 mA in order to reliably estimate the cell parameter of the Co-spinel phase (FullProf.2k software). These patterns were recorded with a step size of 0.026° and a counting time of 2.0 s.

The samples were investigated by Raman spectroscopy with a Renishaw InVia Raman spectrometer, coupled to a Leica DMLM microscope. An ion-argon laser (Modu-Laser, 514 nm) was used while five accumulated scans with a spatial resolution of 2 μm, in a spectral window of 150−900 cm^{-1}, were recorded. X-Ray photoelectron spectroscopy (XPS) measurements were made in a Kratos AXIS Supra spectrometer working with a 225 W Al Kα radiation source and a pass energy of 20 eV.

High Resolution Transmission Electron Microscopy (HRTEM) and Scanning Transmission Electron Microscopy - High Angle Annular Dark Field (STEM-HAADF) images were taken with a Cs-image-corrected Titan (Thermofisher Scientific), which operated at a working voltage of 300 kV, and was equipped with a CCD camera (Gatan) and a HAADF detector (Fischione). A 2k x 2k Ultrascan CCD camera (Gatan) was positioned before the filter for TEM imaging (energy resolution of 0.7 eV). Alternatively, the TEM apparatus could be also connected to an Ultim Max detector (Oxford Instruments) for Energy Dispersive X-ray Spectroscopy (EDX) elemental mapping or a Tridiem Gatan Energy Filter for Electron Energy Loss Spectroscopy (EELS) experiments. These two spectroscopic techniques were useful for obtaining spatially resolved elemental analysis of the samples.

Finally, the redox behaviour of the samples was examined by means of temperature-programmed reduction (H_2-TPR) with a 5%H_2/Ar mixture on a Micromeritics Autochem 2920 apparatus. The experiments were typically carried out in the 50−600 °C temperature range, although occasionally the temperature was increased up to 900 °C. The used heating rate was 10 °C min^{-1}. The catalysts were previously subjected to a cleaning step with a 5%O_2/He mixture at 300 °C for 30 min. Then they were cooled down to 50 °C under inert conditions.

The catalytic behaviour for the complete oxidation of lean methane was examined in a fixed bed quartz tubular reactor in the 200−600 °C temperature range. The composition of the feed stream was 1%CH_4/10%O_2/89%N_2 with a total flow of 100 mL min^{-1}. The composition of the reaction gases was monitored by a SRS RGA200 quadrupole mass spectrometer following the m/z = 44 (CO_2), 32 (O_2), 28 (CO) and 16 (CH_4) signals. The runs were conducted with 300 mg of catalyst (sieve fraction of 0.2−0.3 mm) that were deposited on a glass frit located near the bottom of the reactor tube. This corresponded to a WHSV of 200 mL CH_4 g^{-1} h^{-1} and a GHSV of around 15,000 h^{-1}. Additional catalytic runs were carried out over selected samples at up to 60,000 h^{-1} (800 mL CH_4 g^{-1} h^{-1}). Following the criteria established by Eurokin [32], it was confirmed that inter- and intra-phase concentration and temperature gradients were negligible in all cases (Table S1, Supplementary material). Additionally, the thermal and hydrothermal stability of the most active Co-Ce sample with time on stream was studied at constant temperature (600 °C) and WHSV (200 mL CH_4 g^{-1} h^{-1}) under dry/humid (10 %vol. H_2O) conditions for a total reaction interval of 150 h under, and dry/humid conditions combined with the presence of 10 %vol. CO_2 for 125 h.

3. Results and discussion

3.1. Influence of the Ce/Co molar ratio on the properties and the performance of the Ce-promoted cobalt catalysts supported on α-Al_2O_3

The followed approach to determine the optimal alpha-alumina supported Co-Ce catalytic system for the combustion of lean methane first involved the analysis of a series of samples with a constant reference Co_3O_4 loading (10 %wt.) and a varying Ce/Co molar ratio, between 0 and 0.2 (0, 0.01, 0.03, 0.05, 0.1 and 0.2; 6 samples), which was equivalent to a maximum ceria content of 4.3 %wt.CeO_2. The performance of the synthesised samples was kinetically compared on account of their specific activity at relatively low temperatures (450 °C).

The composition of the samples determined by EDXRF was in accordance with the nominal loading for each metallic element. Table 1 summarises the actual cobalt and cerium loadings expressed in terms of the amount of Co_3O_4 and CeO_2, respectively. The analysis of the textural properties by N_2 physisorption expectedly revealed a low surface area ($4-7$ m^2 g^{-1}). No significant differences were found among the various samples. Accordingly, reduced pore volumes were measured (0.008-0.013 cm^3 g^{-1}). Note that the surface area of the bare alpha-alumina was 5 m^2 g^{-1}. All samples exhibited type III isotherms, characteristic of nonporous or macroporous solids, according to their low specific surface area and pore volume.

The structural properties of the catalysts were evaluated by XRD. The corresponding patterns, including those of the bare support and a bulk Co_3O_4 oxide prepared by calcination of cobalt (II) nitrate hexahydrate at 600 °C, are shown in Fig. S1, Supplementary material. All samples exhibited intense signals associated with a highly crystalline trigonal phase, indexed as alpha-alumina (ICDD 01-081-1667), at $2\theta = 25.7$, 35.5, 37.9, 43.6, 52.8, 57.7, 61.5, 66.7, 68.4 and 76.9°, and low intensity signals of a cubic phase, indexed as cobalt spinel oxide Co_3O_4, at

$2\theta = 19.2$, 31.4, 37.1, 45.0, 59.5 and 65.9° (ICDD 00-042-1467). Moreover, the samples with the largest amounts of cerium, namely the 10Co-2.1Ce and 10Co-4.3Ce catalysts, also displayed a relatively weak signal at $2\theta = 28.6°$, attributable to a cubic phase of segregated CeO_2 (ICDD 00-004-0593). The mean crystallite size of Co_3O_4 included in Table 1 was estimated by applying the Scherrer equation to all the identifiable signals assigned to this oxide phase. No marked differences were observed among the various samples, since the crystallite size was around 36 nm, particularly in the $35-40$ nm range. On the other hand, as indicated by the enlarged view of the diffraction peak at 37.1° (Fig. 1), the signals of cobalt oxide in the Co-Ce catalysts slightly shifted from their positions with respect to the Ce-free cobalt sample. This finding suggested that that the addition of Ce may cause a significant distortion in the spinel structure. In this sense, results included in Fig. 2 and Table 1 evidenced a progressive increase in the cell parameter with the Ce/Co molar ratio. This enlargement, from 8.0960 Å over the Ce-free sample to 8.0971–8.1001 Å over the Co-Ce samples, was explained by the larger ionic radius of Ce^{4+} (101 pm), Ce^{3+} (115 ppm) in comparison with Co^{2+} (79 pm) and Co^{3+} (69 pm). Apparently, the upper limit for cerium atoms that could be inserted into the lattice of Co_3O_4 corresponded to a Ce/Co molar ratio of 0.05 as the largest cell parameter (8.1001 Å) was noticed for the 10Co-1.1Ce catalyst. Above this loading, excess of cerium led to the appreciable formation of segregated CeO_2 with crystallites of around 10 nm in size.

In an attempt to further confirm the distortion of the spinel lattice by cerium, the Co-Ce samples were analysed by Raman spectrometry ($150-900$ cm^{-1}) as well. The corresponding spectra are included in

Table 1
Physico-chemical properties of the Co-Ce catalysts.

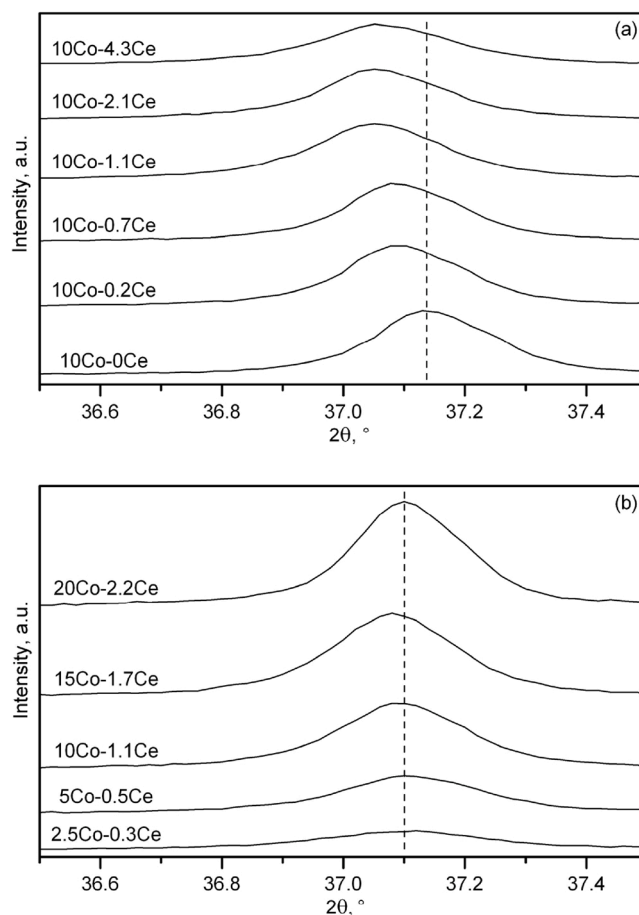| Sample	Ce/Co molar ratio	S_{BET}, m^2 g^{-1}	V_{pore}, cm^3 g^{-1}	DCo_3O_4, nm	Cell parameter, Å	H_2 uptake, mmol $gCo_3O_4^{-1}$
α-Al_2O_3	–	4.8	0.007	–	–	–
Co(10)-Ce(0)	0	4.0	0.007	40	8.0960	16.6
Co(10)-Ce(0.2)	0.01	4.4	0.008	38	8.0971	17.1
Co(10)-Ce(0.7)	0.03	5.2	0.009	37	8.0978	17.4
Co(10)-Ce(1.1)	0.05	5.7	0.013	35	8.1001	17.4
Co(10)-Ce(2.1)	0.10	5.7	0.010	35	8.0997	17.7
Co(10)-Ce(4.3)	0.20	6.6	0.010	34	8.0989	17.9
Co(2.5)-Ce(0.3)	0.05	5.1	0.009	25	8.1005	17.2
Co(5)-Ce(0.5)	0.05	5.3	0.011	30	8.1005	17.2
Co(15)-Ce(1.7)	0.05	6.0	0.014	39	8.1011	17.3
Co(20)-Ce(2.2)	0.05	5.8	0.012	40	8.1015	17.5

Fig. 1. Close-up view of the XRD profiles (35-39° 2θ range) of the Co-Ce catalysts. (a) samples with varying Ce/Co molar ratio and a fixed Co_3O_4 loading (10 %wt.), (b) samples with varying Co loading and a fixed Ce/Co molar ratio (0.05).
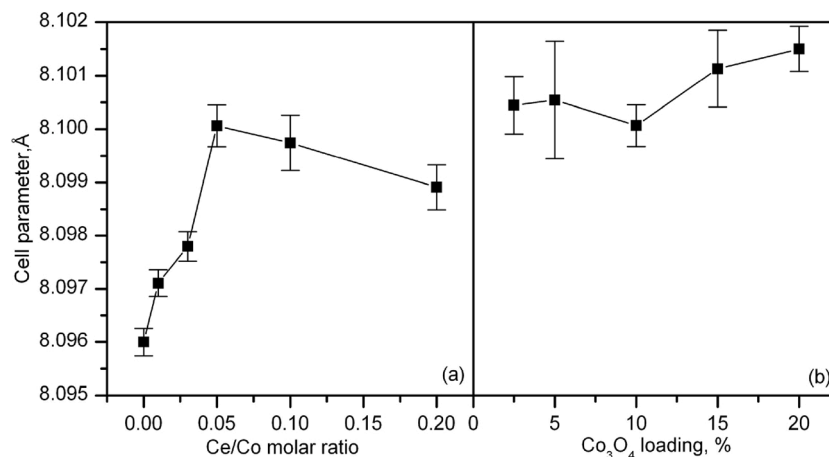
Fig. 2. Evolution of the cell parameter with the composition of the Co-Ce catalysts. (a) samples with varying Ce/Co molar ratio and a fixed Co_3O_4 loading (10 %wt.), (b) samples with varying Co loading and a fixed Ce/Co molar ratio (0.05).
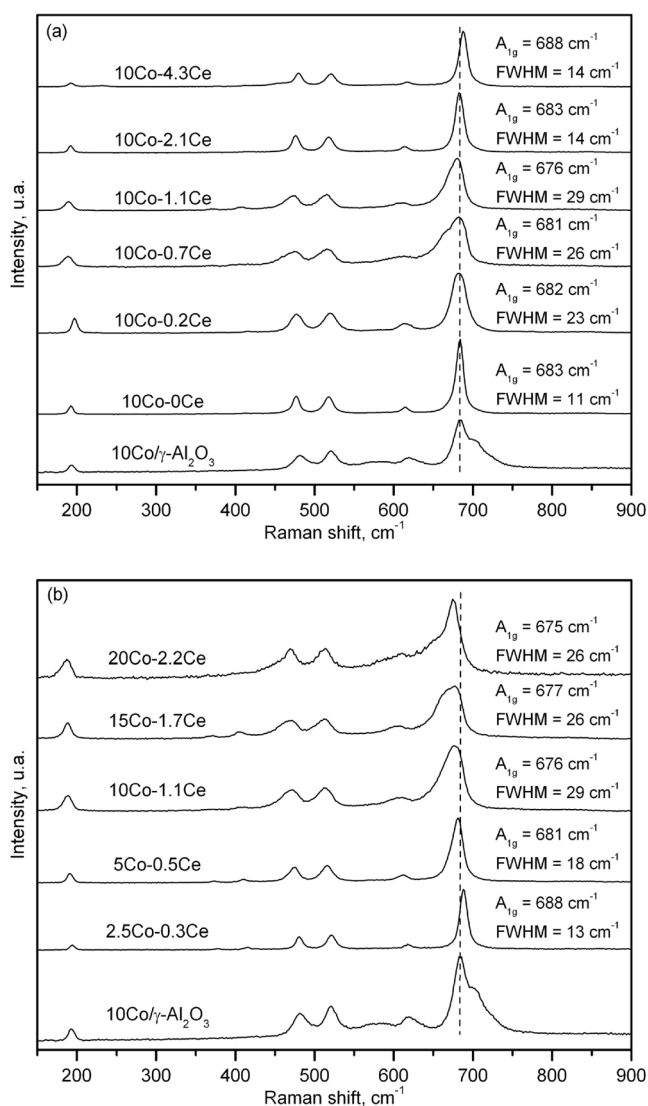

Fig. 3. Raman spectra of the Co-Ce catalysts. (a) samples with varying Ce/Co molar ratio and a fixed Co_3O_4 loading (10 %wt.), (b) samples with varying Co loading and a fixed Ce/Co molar ratio (0.05).

Fig. 3. The spectrum of the 10Co-0Ce was typical of Co_3O_4 with several bands assignable to the F_{2g} mode (194, 519 and 617 cm^{-1}), and two bands attributable to the E_g and A_{1g} modes (479 and 687 cm^{-1}), respectively [33]. It is worth emphasising that the shoulders at 705 and 725 cm^{-1} attributable to the presence of $CoAl_2O_4$ [34] were apparently not observed. In contrast, the spectrum of a sample with a comparable Co_3O_4 content but supported on gamma-alumina (12 %wt. Co_3O_4/γ-Al_2O_3 named as 10Co/Al(γ), 138 $m^2 g^{-1}$) clearly exhibited these two features, thereby suggesting the formation of this undesired cobalt phase due to the strong interaction between Co_3O_4 and γ-Al_2O_3. The cobalt samples with Ce also showed these same five Raman bands, but they changed appreciably from their original positions and exhibited broader shapes and a marked asymmetry. Thus, as also revealed by XRD, the Co_3O_4 lattice certainly seemed to be modified by cerium addition. The intense A_{1g} band therefore shifted from 683 cm^{-1} over the 10Co-0Ce sample to 676 cm^{-1} over the 10Co-1.1Ce sample. More remarkably, a relatively higher FWHM (Full Width Half Maximum), between 14 and 29 cm^{-1}, were consistently found in relation to that of the catalyst without Ce (11 cm^{-1}). The highest value was noted for the 10Co-1.1Ce sample, thereby pointing out that the largest extent of lattice distortion occurred for this catalyst. A higher Ce/Co molar ratio (namely, 0.1 and 0.2) did not lead to appreciable structural changes of the spinel lattice as dictated by the same position of the A_{1g} band and FWHM, when compared with the unpromoted cobalt catalyst. As for the possible generation of stable $CeAlO_3$ due to the interaction of deposited cerium with the alumina support, it should be stated that, in line with the low propensity of alpha alumina supported Co catalysts to form cobalt aluminate, the formation of this perovskite was not expected owing to the high chemical stability and the low surface area of α-Al_2O_3 support, the relatively low cerium content of the samples and the net-oxidising nature of the feedstream at the reactor inlet (1% $CH_4/10O_2/N_2$). As will be shown later, it is worth pointing out that even submitting the Co-Ce catalysts to a thermal treatment up to 850 °C under reducing conditions, the H_2 uptake expected at these high temperatures assignable to $CeAlO_3$ ($2CeO_2 + Al_2O_3 + H_2 \rightarrow 2CeAlO_3 + H_2O$) was not observed.

XPS measurements could be also useful in obtaining detailed information on the relative abundance of the reducible species on the catalyst surface. The Co2p spectra were characterised by broad signals, which suggested the presence of various cobalt species with different oxidation state. In particular, the Co $2p_{3/2}$ signal could be deconvoluted into five contributions (Fig. S2, Supplementary material). Thus, the two main contributions located at around 779.5 and 780.7 eV were attributed to Co^{3+} and Co^{2+} ions respectively, while the two bands at higher binding energies (785.5 and 789.5 eV) were associated with the satellite signals from Co^{2+} and Co^{3+} ions, respectively [35]. Finally, the signal centred at

782.2 eV was related to the presence of CoO species [36], which was the consequence of the decomposition of the spinel cobalt oxide under vacuum conditions [37]. The contribution of this oxide was quite similar on all samples, about 5–10 % of the total amount of cobalt. The O1s spectra exhibited two signals at 529.8 and 530.8 eV, respectively (Fig. S2, Supplementary material). The former was related to oxygen ions of the lattice (O_{latt}) whereas the latter was adscribed to adsorbed oxygen species on the surface (O_{ads}) [38,39]. On the other hand, due to the relative low Ce concentration of the samples, the deconvolution of the Ce 3d spectra (880−916 eV) was not possible, and therefore the relative abundance of Ce^{4+} and Ce^{3+} species could not reliably estimated. However, at least it was possible to quantify the total the total concentration of Ce. Thus, XPS analysis evidenced a noticeably variation in the relative abundance of cobalt and cerium at the surface level when compared with the bulk composition. Hence, while the surface cobalt content gradually decreased from 10.3 %wt. (10Co-Ce0) to around 6.4 %wt. (10Co-4.3Ce), a substantial Ce enrichment varying between 2.7 and 8.4 %wt. was noticed simultaneously. Recall that the corresponding cerium bulk concentration was in the 0.3–4.3 %wt. range. As a result, the Ce/Co molar ratio at the surface increased 10−20 times with respect to the corresponding bulk value.

Both Co^{3+}/Co^{2+} and O_{ads}/O_{latt} molar ratios could be estimated from the quantification of the corresponding areas of the signals (Table 2). A direct correlation was found between the presence of Co^{3+} species and the abundance of lattice oxygen species [40,41]. The addition of cerium, presumably as Ce^{4+}, resulted in a favoured presence of Co^{3+} at the cost of Co^{2+} as revealed by the significantly high Co^{3+}/Co^{2+} molar ratios, which ranged from 0.91 for the Ce-free sample to around 1.2 over the 10Co-1.1Ce catalyst (Fig. 4). This Co^{3+} enrichment was rationalised by the $Ce^{4+} + Co^{2+} \leftrightarrow Ce^{3+} + Co^{3+}$ equilibrium that established the balance charge within the cations of the spinel lattice [42]. Above this Ce loading, the relative abundance of Co species did not markedly vary in line with the fact that Ce insertion into the Co_3O_4 lattice was no longer activated with higher Ce contents. As aforementioned, the abundance of Co^{3+} species was directly related to the presence of lattice oxygen species with decreasing O_{ads}/O_{latt} molar ratios from around 0.4 over the 10Co-0Ce catalyst to about 0.1 for the 10Co-1.1Ce, 10Co-2.1Ce and 10Co-4.3Ce catalysts. On the other hand, the difference in surface composition between the Ce-free catalysts supported on α-Al_2O_3 and γ-Al_2O_3 was also notable. Therefore, the appreciable presence of cobalt aluminate in the 10Co/Al(γ) sample, as suggested by Raman spectroscopy, led to a markedly lower Co^{3+}/Co^{2+} molar ratio (0.29) in

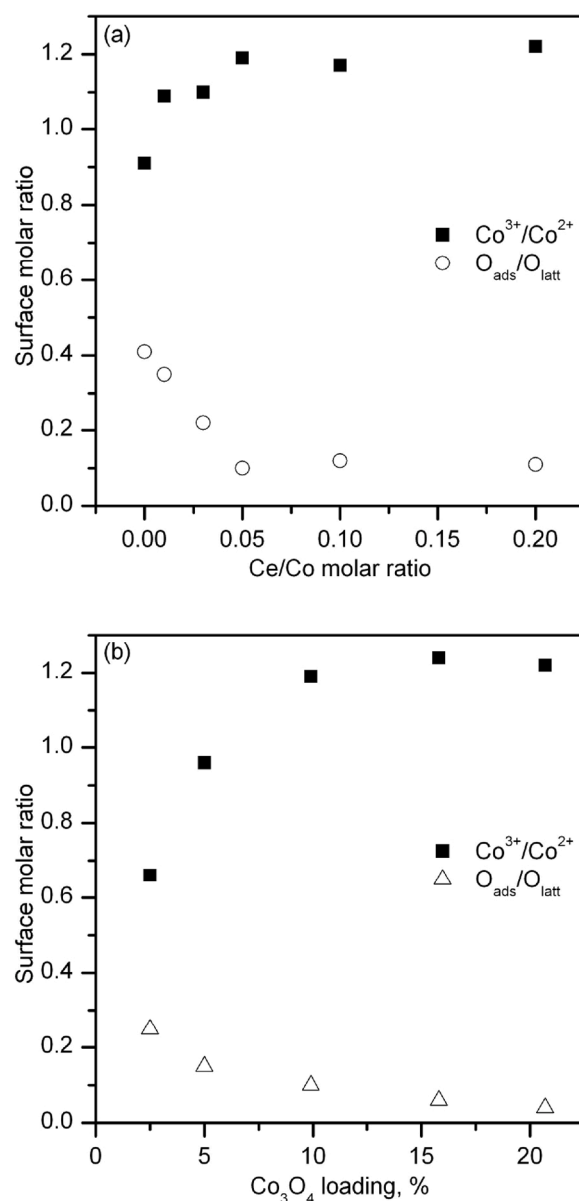**Fig. 4.** Relationship of the surface composition (Co^{3+}/Co^{2+} and O_{ads}/O_{latt} molar ratio as determined by XPS) with the bulk composition of the Co-Ce catalysts (as determined by EDXRF). (a) samples with varying Ce/Co molar ratio and a fixed Co_3O_4 loading (10 %wt.), (b) samples with varying Co loading and a fixed Ce/Co molar ratio (0.05).

comparison with the counterpart supported on alpha-alumina support (0.91). Accordingly, the abundance of lattice oxygen species was higher over the 10Co-0Ce catalyst (0.41 versus 1.99 over the 10Co/Al(γ) sample). In sum, the observed increase in the Co^{3+}/Co^{2+} ratio with cerium loading could be rationalised in terms of the insertion of Ce ions into the lattice of the cobalt spinel. This insertion was evidenced by the distortion of the framework revealed by the significant enlargement of the Co_3O_4 cell parameter accompanied by a notable widening (FHWM) of the main Raman vibration signal (A_{1g}, particularly in the lower frequency region), as shown in Fig. S3, Supplementary material. This insertion seemed to be favoured for Ce/Co molar ratios up to 0.05, with higher values not inducing any further enlargement of the cell parameter and modification of FHWM of the Raman mode.

An attempt was made to obtain a more defined view of the surface chemical structure using scanning transmission electron microscopy–high-angle annular dark field (STEM–HAADF). Additionally,
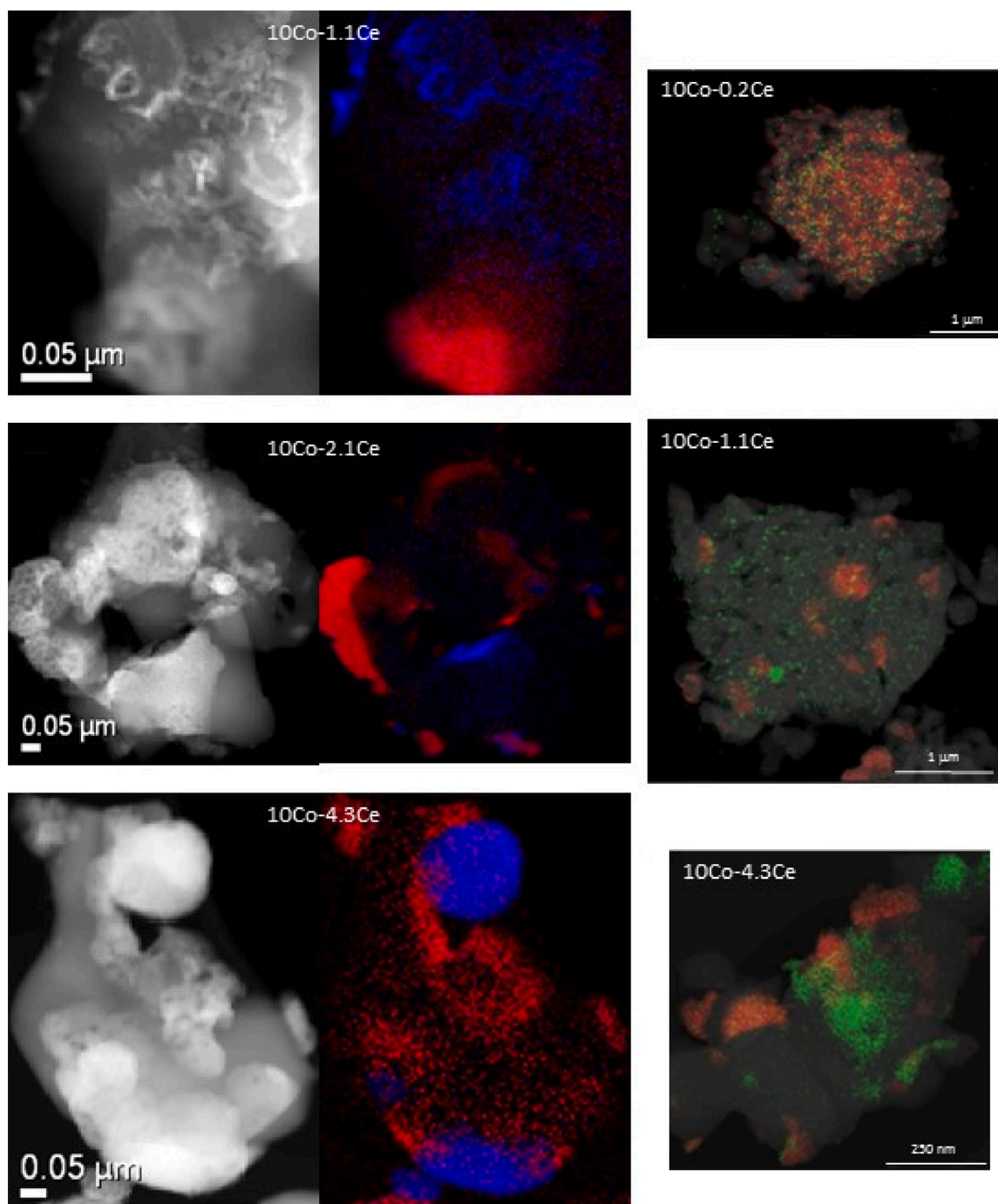
Table 2
Surface composition of the Co-Ce catalysts.

Sample	Co content, %wt.	Ce content, %wt.	Co^{3+}/Co^{2+} molar ratio	O_{ads}/O_{latt} molar ratio
Co(10)-Ce (0)	10.3 (7.4)	0 (0)	0.91	0.41
Co(10)-Ce (0.2)	8.1 (7.4)	2.7 (0.2)	1.09	0.35
Co(10)-Ce (0.7)	6.7 (7.4)	5.8 (0.6)	1.10	0.22
Co(10)-Ce (1.1)	7.0 (7.4)	6.7 (0.9)	1.19	0.10
Co(10)-Ce (2.1)	7.4 (7.4)	7.7 (1.7)	1.17	0.12
Co(10)-Ce (4.3)	6.4 (7.4)	8.4 (3.5)	1.22	0.11
Co(2.5)-Ce (0.3)	4.2 (1.9)	4.3 (0.2)	0.66	0.25
Co(5)-Ce (0.5)	6.1 (3.7)	6.5 (0.4)	0.96	0.15
Co(15)-Ce (1.7)	10.3 (11.6)	9.7 (1.4)	1.24	0.06
Co(20)-Ce (2.2)	12.9 (15.2)	10.1 (1.8)	1.22	0.04

Values in parentheses correspond to the equivalent loadings of Co_3O_4 and CeO_2.

Fig. 5. STEM-HAADF images and EDX and EELS maps of selected Co-Ce catalysts with varying Ce/Co molar ratio and a fixed Co_3O_4 loading (10 %wt.). (Red) cobalt and (blue) cerium for EELS maps (left); (red) cobalt and (green) cerium for EDX maps (right).

representative EDX and EELS elemental maps (Fig. 5) were taken from selected samples (namely 10Co-0.2Ce, 10Co-1.1Ce, 10Co-2.1Ce and 10Co-4.3Ce catalysts) to determine the effect of the Ce/Co molar ratio on the spatial distribution of both metals. Cerium was found to be homogenously mixed with cobalt in the 10Co-0.2Ce and 10Co-1.1Ce samples, preferably in the form of highly dispersed crystallites less than 5 nm in size. It was also true that crystallites between 10−20 nm could occasionally be found on the surface of the 10Co-1.1Ce catalyst. In contrast, the 10Co-2.1Ce sample more abundantly presented clusters with a significantly larger size around 20−25 nm, while the 10Co-4.3Ce sample contained patches as large as 100−150 nm, which were formed by the apparent agglomeration of smaller crystallites. These

observations evidenced the low dispersion of cerium species on these two Ce-rich catalysts. On the other hand, the size of Co_3O_4 was not greatly affected by the amount of added cerium, with an average size between 35−50 nm. The samples were also investigated by HRTEM. As an example, Fig. S4, Supplementary material includes typical HRTEM images of the 10Co-2.1Ce catalyst. The characteristic lattice fringes with interplanar spacing of 0.244 and 0.286 nm assignable to the {311} and the {220} planes of the Co_3O_4 phase were identified. Likewise, two lattice spaces of 0.31 and 0.27 nm were evidenced, which corresponded to the {111} and {200} planes of CeO_2, respectively.

Finally, the redox properties of the samples were investigated by H_2-TPR. The corresponding profiles are shown in Fig. 6. For comparative
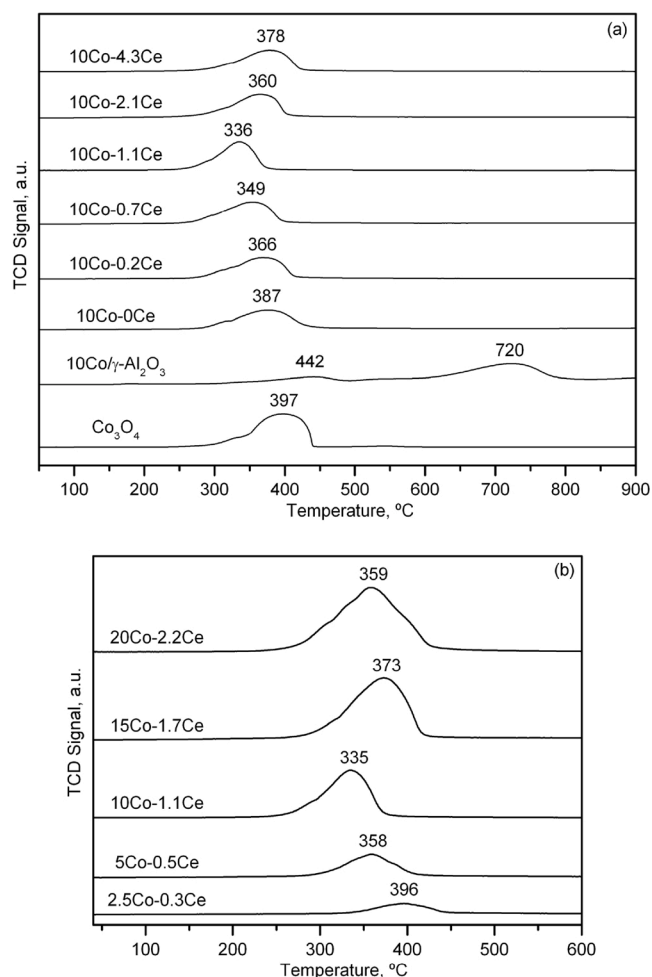
Fig. 6. H$_2$-TPR profiles of the Co-Ce catalysts. (a) samples with varying Ce/Co molar ratio and a fixed Co$_3$O$_4$ loading (10 %wt.), (b) samples with varying Co loading and a fixed Ce/Co molar ratio (0.05).

purposes, the traces corresponding to a bulk Co$_3$O$_4$ oxide (prepared by direct calcination of cobalt nitrate at 600 °C) and a Co$_3$O$_4$ catalyst supported on gamma alumina (12 %wt.Co$_3$O$_4$/γ-Al$_2$O$_3$, 10Co/Al(γ) sample) are included as well. Typically, the reduction of the Co$_3$O$_4$ phase is a two-step process that involves the consecutive reduction of Co^{3+} to Co^{2+} at low temperatures and the reduction of Co^{2+} to metallic cobalt at high temperatures [43]. The profile of the reference Ce-free cobalt catalyst (10Co-0Ce) showed a main reduction band at 375 °C, with a barely perceptible shoulder at lower temperatures (325 °C). No H$_2$ uptake was detected above 450 °C, which was in agreement with the full reduction of cobalt species as Co$_3$O$_4$, since the experimental consumption was 16.6 mmol H$_2$ g$_{Co3O4}^{-1}$. It could be therefore confirmed that this sample supported on alpha alumina did not contain appreciable amounts of highly stable cobalt species in the form of cobalt aluminate. This was in contrast with the results obtained with the analogous counterpart supported on gamma alumina (10Co/Al(γ)), in which a substantially high fraction of deposited cobalt species (around 90 %) were converted to CoAl$_2$O$_4$ due to the partial dissolution to Co$_3$O$_4$ into the γ-Al$_2$O$_3$ lattice, as revealed by its marked H$_2$ uptake at temperatures higher than 500 °C (Fig. 6). Accordingly, its total consumption was only 17.7 mmol H$_2$ g$_{Co}^{-1}$, significantly lower than the theoretical value corresponding to the exclusive presence of Co$_3$O$_4$ (22.6 mmol H$_2$ g$_{Co}^{-1}$).

As the amount of cerium in the catalyst increased, the reducibility was enhanced since a progressive shift in peak reduction temperatures was visible, from 390 °C (10Co-0Ce) to 335 °C over the sample with a Ce/Co molar ratio of 0.05 (1.1 %wt.CeO$_2$). These results were in

agreement with the higher Ce dispersion evidenced by STEM-HAADF coupled to EDX and EELS. Above this molar ratio (0.1 and 0.2), the promotion of reducibility was somewhat less evident, with peak reduction temperatures of about 360−375 °C. The promotion of the redox properties with the Ce/Co molar ratio up to 0.05 was also evident when analysing the onset temperatures for reduction. This was as low as 190 °C for the 10Co-1.1Ce catalyst whilst it varied between 210−240 °C for other Ce loadings. The onset reduction temperature for the Ce-free 10Co-0Ce sample was 240 °C. The observed increase in the H$_2$ uptake at low temperatures could be rationalised in terms of a favoured reduction of Co$_3$O$_4$ with a distorted lattice due to cerium doping as revealed by XRD, Raman spectroscopy and XPS analysis. On the other hand, the overall H$_2$ uptakes increased with the cerium content from 1.6 to 1.8 mmol H$_2$ g^{-1} (which was equivalent to 17.1–17.9 mmol H$_2$ g$_{Co3O4}^{-1}$), thereby revealing an greater contribution of the present cerium species to the overall reducibility of the catalysts (Table 1). Note that ceria reduction could be activated due to transfer of hydrogen by metallic cobalt onto its surface [44].

The corresponding light-off curves of this series of cobalt catalysts modified with cerium as a promoter are shown in Fig. 7 (200 mL CH$_4$ g^{-1} h^{-1}). All studied cobalt catalysts exhibited 100 % CO$_2$ selectivity. The observed efficiency could be classified into two groups with a substantially different performance. On one hand, the samples with a
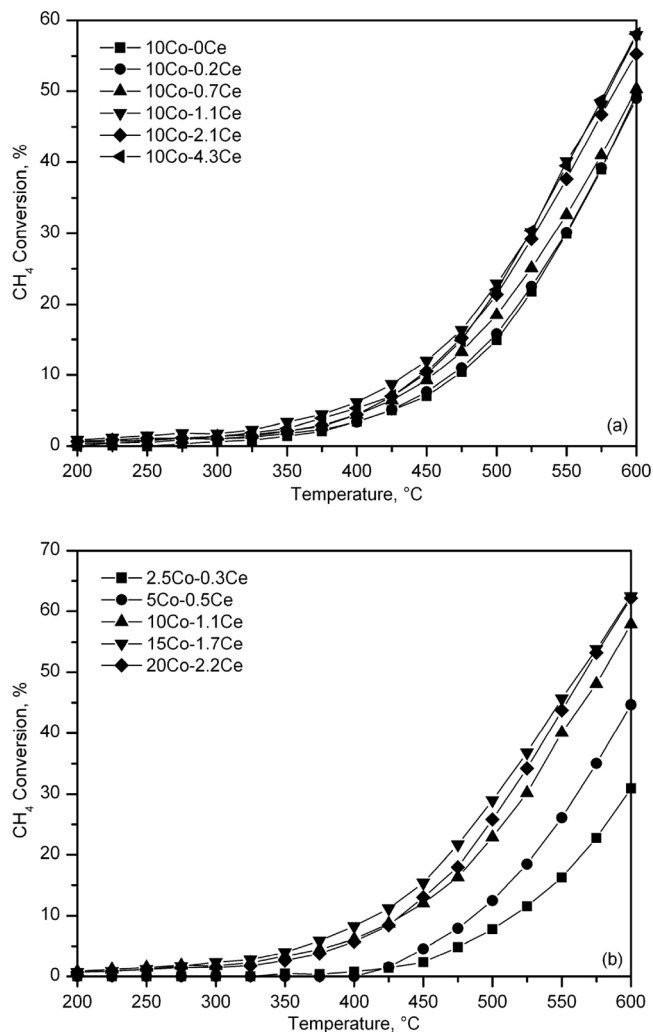

Fig. 7. Light-off curves of the oxidation of trace amounts of methane at 15,000 h^{-1} over the Co-Ce catalysts. (a) samples with varying Ce/Co molar ratio and a fixed Co$_3$O$_4$ loading (10 %wt.), (b) samples with varying Co loading and a fixed Ce/Co molar ratio (0.05).

Ce/Co molar ratio of 0, 0.01 and 0.03 exhibited a similar (540−550 °C) T_{30} (temperature at which 30 % conversion was attained) and a conversion as low as 17 % at 600 °C. On the other hand, the 10Co-1.1Ce, 10Co-2.1Ce/Al and 10Co-4.3Ce catalysts showed a significantly lower T_{30} (520−530 °C) with a conversion of 55 % at 600 °C. Thus, the efficiency was promoted with the incorporation of cerium but above 1.1 % wt. (corresponding to a Ce/Co molar ratio of 0.05) no further improvement was attained. Recall that the intrinsic activity of pure CeO_2 was negligible in the investigated temperature window (200−600 °C) [18].

The catalytic benefits of cerium addition were best evidenced when analysing the relationship of the resultant Co^{3+}/Co^{2+} and O_{ads}/O_{latt} molar ratios with the specific reaction rate at 450 °C (Fig. 8 and Table 3). A promotion of the catalytic activity was progressively observed with the higher abundance of Co^{3+} species, which in turn was connected to a favoured presence of oxygen lattice species. Hence, the specific reaction rate increased from 0.24 mmol CH_4 g^{-1} h^{-1} over the Ce-free sample (with a Co^{3+}/Co^{2+} molar ratio of 0.9) to 0.41 mmol CH_4 g^{-1} h^{-1} over the 10Co-1.1Ce catalyst (with a Co^{3+}/Co^{2+} molar ratio of 1.2). No significant enhancement was noticed with the catalysts with a higher Ce content, since the reaction rate remained relatively constant (0.35−0.36 mmol CH_4 g^{-1} h^{-1}) in coherence with their similar $Co^{3+}/$

Table 3
Kinetic results of the Co-Ce catalysts for the oxidation of lean methane.

Catalyst	T_{30}, °C	Specific reaction rate, mmol CH_4 g^{-1} h^{-1}	Specific reaction rate, mmol CH_4 g_{Co3O4}^{-1} h^{-1}	Apparent activation energy, kJ mol^{-1}
Co(10)-Ce (0)	550	0.24	2.4	93 ± 1
Co(10)-Ce (0.2)	550	0.26	2.6	79 ± 1
Co(10)-Ce (0.7)	540	0.32	3.2	76 ± 1
Co(10)-Ce (1.1)	520	0.41	4.1	72 ± 2
Co(10)-Ce (2.1)	530	0.36	3.6	71 ± 2
Co(10)-Ce (4.3)	530	0.35	3.5	71 ± 3
Co(2.5)-Ce (0.3)	595	0.07	2.9	93 ± 1
Co(5)-Ce (0.5)	560	0.17	3.3	85 ± 2
Co(15)-Ce (1.7)	510	0.52	3.3	72 ± 2
Co(20)-Ce (2.2)	510	0.45	2.2	71 ± 2

Co^{2+} relative distribution (around 1.2). The optimal behaviour of the 10Co-1.1Ce catalyst was also determined by plotting the specific reaction rate normalised to the total amount of cobalt as Co_3O_4 and T_{30} as a function of the Ce/Co molar ratio (Fig. S5, Supplementary material). This sample indeed contained highly mobile oxygen species as revealed by the lower peak reduction temperatures [45]. In sum, the interaction between Co_3O_4 and CeO_2 was essential for an improved catalytic performance in the oxidation of methane [46,47]. The optimal Ce/Co molar ratio was defined at 0.05. Higher Ce/Co molar ratios forced the cerium species to segregate from the spinel lattice and did not lead to any significant improvement in activity.

The apparent activation energies of the supported Co-Ce catalysts (Table 3) were in the 71−76 kJ mol^{-1} range, comparable to that of pure Co_3O_4 [48,49]. A first pseudo-order for methane and a zeroth pseudo-order for oxygen were assumed. The resultant kinetic equation was coherent with Mars–van Krevelen kinetics in the presence of excess oxygen [50,51]. Then, the linearised equation of the integral reactor was plotted by using conversions between 10–65 % (Fig. S6, Supplementary material). Unexpectedly, the 10Co-Ce0.2, and particularly the Ce-free 10Co-0Ce, samples showed higher apparent activation energies, namely 79 and 93 kJ mol^{-1}. This finding suggested that the kinetic behaviour was partially controlled by the presence of less active phases than Co_3O_4. Although the characterisation results of these two samples by Raman spectroscopy and H_2-TPR did not evidence the existence of cobalt aluminate, it was also true that the surface Co^{3+}/Co^{2+} molar ratio was particularly low (0.9–1.1 compared with about 1.2 over the samples with a higher Ce content), which would be consistent with the presence of traces amounts of highly dispersed cobalt aluminate along with cobalt oxide. It is worth remarking that the apparent activation energy of the $CoAl_2O_4$-rich Co_3O_4 catalyst (10Co/Al(γ)) was around 100 kJ mol^{-1} [22], not far from the estimated values of the 10Co-0.2Ce and 10Ce-0Ce catalysts. Accordingly, Fan et al. [52] have recently reported values ranging 92−109 kJ mol^{-1} over a series of $CoAlOx/CeO_2$ catalysts.

3.2. Influence of the Co_3O_4 loading on the properties and performance of the Ce-promoted cobalt catalysts supported on α-Al_2O_3

Next, the effect of the Co_3O_4 loading on the physico-chemical properties and the performance of the supported Co-Ce catalysts were examined while keeping constant their Ce/Co molar ratio at the previously defined optimal value (0.05). Hence, a series of samples with a Co_3O_4 loading varying in the 2.5−20 wt% range (2.5, 5, 10, 15 and 20; 5
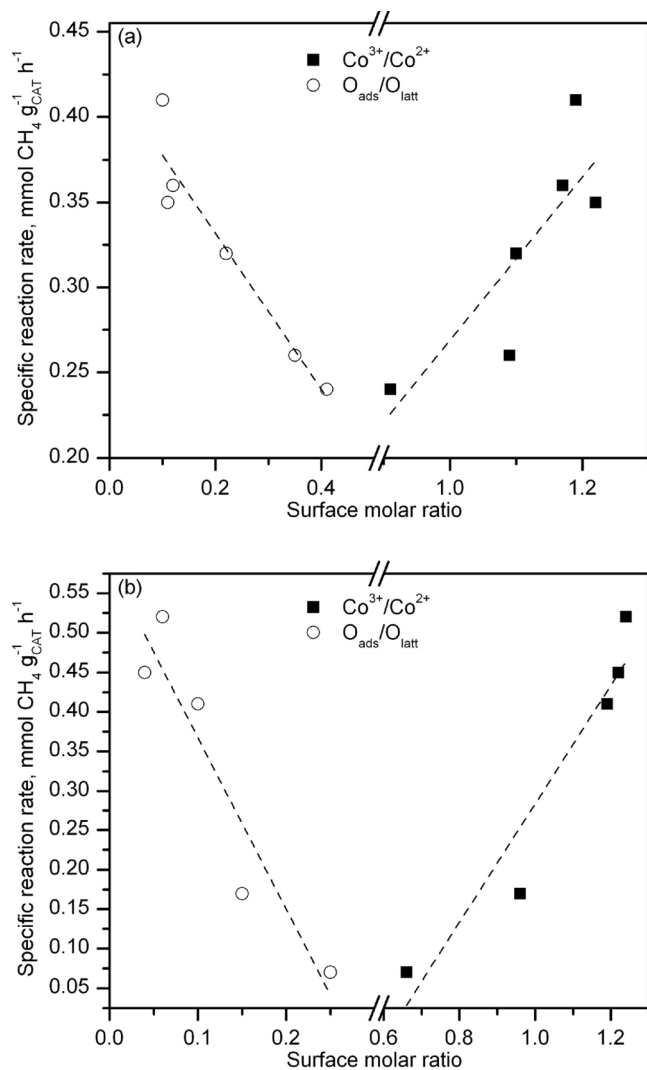

Fig. 8. Relationship between the specific reaction rate and surface composition of the Co-Ce catalysts. (a) samples with varying Ce/Co molar ratio and a fixed Co_3O_4 loading (10 %wt.), (b) samples with varying Co loading and a fixed Ce/Co molar ratio (0.05).

samples) and this fixed Ce/Co molar ratio was prepared. The corresponding composition and textural properties are listed in Table 1. The ceria content of the samples accordingly varied between 0.3–2.2 %wt. Both surface areas and pore volumes were expectedly low (5–6 $m^2 g^{-1}$ and $0.008-0.013$ $cm^3 g^{-1}$, respectively), with no relevant differences among the various samples.

Analogously to the previous results, the XRD patterns also evidenced the signals corresponding to the α-Al_2O_3 (ICDD 01-081-1667), Co_3O_4 (ICDD 00-042-1467) and CeO_2 (ICDD 00-004-0593) phases (Fig. S1, Supplementary material). Segregated ceria (with crystallites around 10 nm in size) was only detected over the 15Co-1.7Ce and 20Co-2.2Ce samples. On the other hand, the relative intensity of the signals of the cobalt spinel and alumina constantly increased with Co_3O_4 loading. The mean crystallite size of Co_3O_4, as estimated by the Scherrer equation, depended notably on the cobalt content (Table 1). Hence, this was 25 nm for the 2.5Co-0.3Ce catalyst, gradually growing to a reasonably constant value of around 40 nm for the samples with the highest cobalt loadings (15 and 20 %wt.Co_3O_4). It is worth pointing out that the location of the main diffraction signal at 2θ at $37.1°$ did not vary notably with Co content (Fig. 1). Accordingly, as shown in Fig. 2 the difference in the cell parameter (0.0014 Å) was less noticeable when compared with the set of samples with varying Ce/Co molar ratio and a fixed amount of Co_3O_4 (10 %wt.), with a maximum deviation of 0.0041 Å. This suggested that the extent distortion provoked by the insertion of Ce ions into the spinel lattice was relatively similar regardless of the cobalt content. These results were coherent with those derived from Raman spectroscopy (Fig. 3). Thus, the position of the A_{1g} band shifted towards lower values, from 688 cm^{-1} over the 2.5Co-0.3Ce to $675-677$ cm^{-1} for the samples with a Co loading between $10-20$%wt.Co_3O_4. Hence, a similar FWHM about $26-29$ cm^{-1} was observed over the catalysts with a Co loading of $10-20$%wt.Co_3O_4, which were characterised by a relatively large crystallite size close to 40 nm. Apparently, the crystallites ($25-30$ nm) of the 2.5Co-0.3Ce and 5Co-0.5Ce samples seemed to be somewhat more resistant to cell distortion by Ce doping judging from their reduced FHWM (13-18 cm^{-1}).

The Co2p XPS spectra of these catalysts (Fig. S2, Supplementary material) presented the same five contributions previously described for the first set of samples. However, in this case, the relative intensity of the spectra varied appreciably among the samples, in agreement with their increased cobalt loading. Besides, the intensity ratio between the two main contributions (centred at around 779.5 and 780.7 eV and attributed to Co^{3+} and Co^{2+} ions, respectively) increased significantly with the cobalt loading, thus evidencing a more predominant presence of Co^{3+} ions (Table 2). Thus, Co^{2+} ions were the prevailing species in the catalysts with a lower Co loading. On the other hand, a greater abundance of lattice oxygen species was found for the 10Co-1.1Ce, 15Co-1.7Ce and 20Co-2.2Ce samples (Fig. S2, Supplementary material). Therefore, as evidenced by the results summarised in Fig. S3 (Supplementary material), the catalysts with a lower cobalt content (2.5 and 5% wt.) exhibited highly stable Co_3O_4 crystallites that were hardly affected by the presence of cerium since the observed changes in both cell parameter and FWHM were less significant. For higher cobalt loadings, cerium atoms seemed to effectively insert into the Co_3O_4 lattice resulting in a more marked enlargement of the cell size with a concomitant higher asymmetry of the A_{1g} Raman mode, which finally resulted in a higher abundance of Co^{3+} species.

The analysis of the surface composition of these samples also revealed important discrepancies with respect to the bulk composition, in line with what occurred with the set of catalysts with varying Ce/Co molar ratio (Table 2). In this sense, the surface Ce loadings were about $10-20$% higher than the nominal bulk loadings for all the examined catalysts. The surface Co content, on the other hand, varied from being 2 times higher than the bulk composition for the catalysts with lower loadings (2.5Co-0.3Ce and 5Co-0.5Ce) to being slightly lower than the bulk composition for the Co-rich catalysts. This could be due to the low dispersion of the cobalt oxide crystallites in catalysts with higher cobalt

loadings, as will be shown later by electronic microscopy. The cobalt oxide content also had a marked effect on the surface species distribution. The 2.5Co-0.3Ce and 5Co-0.5Ce catalysts presented lower Co^{3+}/Co^{2+} molar ratios (0.66 and 0.96, respectively) than those with higher loadings, which were between 1.19 and 1.24. In fact, for the samples with $10-20$%wt.Co_3O_4 the Co^{3+}/Co^{2+} molar ratio did not vary appreciably. In consonance with the previous findings, the higher abundance of Co^{3+} species was accompanied by decreasing O_{ads}/O_{latt} molar ratios, thus showing a more predominant presence of lattice oxygen species (Fig. 4).

On the other hand, the effect of Co_3O_4 loading on cobalt dispersion was examined by STEM–HAADF with the simultaneous acquisition of EDX and EELS elemental maps of certain samples, namely 2.5Co-0.3Ce, 5Co-0.5Ce, 10Co-1.1Ce, 15Co-1.7Ce and 20Co-2.2Ce (Fig. 9). Some of these catalysts (5Co-0.5Ce and 15Co-1.7Ce samples) were complementarily characterised by HRTEM (Fig. S4, Supplementary material). In general, the catalysts with Co_3O_4 loadings up to 15 %wt. revealed crystallites with sizes varying between 35 and 55 nm. These values were in line with those measured by XRD (between 30 and 40 nm). In the case of the 2.5Co-0.3Ce and 5Co-0.5Ce samples crystallites with sizes as small as 20 nm were detected as well. Likewise, these catalysts also presented regions covered by extremely small cobalt-containing crystallites (<5 nm) that were highly dispersed on the surface of the alpha-alumina and were not part of any large cluster. As will be suggested later, this good Co coverage could lead to the formation of some surface cobalt aluminate-like species in these regions. In contrast, visible Co_3O_4 particles in the 20Co-2.2Ce sample presented a much broader size distribution ranging from 40 to 130 nm, this revealing a massive aggregation of crystallites. Finally, it should be mentioned that the dispersion of cerium in all samples was comparable and relatively high, in line with their same Ce/Co molar ratio (0.05).

The H_2-TPR profiles (Fig. 6) of the catalysts with the lowest cobalt content, namely the 2.5Co-0.3Ce and 5Co-0.5Ce samples, were characterised by a dominant uptake peaking at 395 and 360 °C, respectively. A clear distinction of the stepwise reduction process of Co_3O_4 was not evident [53]. For higher metal loadings (10, 15 and 20 %wt.) a shoulder located at lower temperatures ($290-320$ °C) could be ascertained. In the same way as seen previously for the first set of Co-Ce catalysts, the massive presence of highly stable cobalt species in the supported catalysts, with an expected reduction temperature exceeding 500 °C, was ruled out. Likewise, the formation of the $CeAlO_3$ perovskite during the analysis was not observed. Relatively high peak reduction temperatures were found for the Co-poor catalysts (400 and 350 °C over the 2.5Co-0.3Ce and 5Co-0.5Ce samples, respectively). This could be ascribed to their high dispersion as determined by STEM-HAADF. Hence, the reducibility was promoted with larger crystallite sizes since the H_2 uptake peaked at 335 °C for the 10Co-1.1Ce sample with a mean size of 35 nm. Above this size the reduction temperatures shifted to $360-375$ °C (15Co-1.7Ce and 20Co-2.2Ce), probably due to the fact that a significant fraction of cobalt was present as segregated Co_3O_4 (not deposited on the alumina support). This optimal redox behaviour of the 10Co-1.1Ce catalyst was also evidenced by its lower reduction onset temperature (around 280 °C). On the other hand, the contribution of cerium species to the redox behaviour of the catalysts was significant with an overall specific H_2 consumption in the 17.2–17.5 mmol g_{Co3O4}^{-1} range, which was superior to that expected to the exclusive reduction of Co_3O_4. As aforementioned, this excess of H_2 uptake was attributed to the contribution of the reduction of the cerium cations, which in turn can be activated by metallic cobalt.

The light-off curves of the combustion of methane over this set of Co-Ce catalysts are included in Fig. 7. 100 % CO_2 selectivity was always noticed. Clearly, samples with a relatively low Co loading (2.5Co-0.3Ce and 5Co-0.5Ce samples) evidenced a poorer performance with T_{30} between $560-595$ °C (Table 3). A remarkably higher efficiency was observed over the samples with 10, 15 and 20 %wt.Co_3O_4, although no notable differences among these three catalysts. Hence, T_{30} was in the
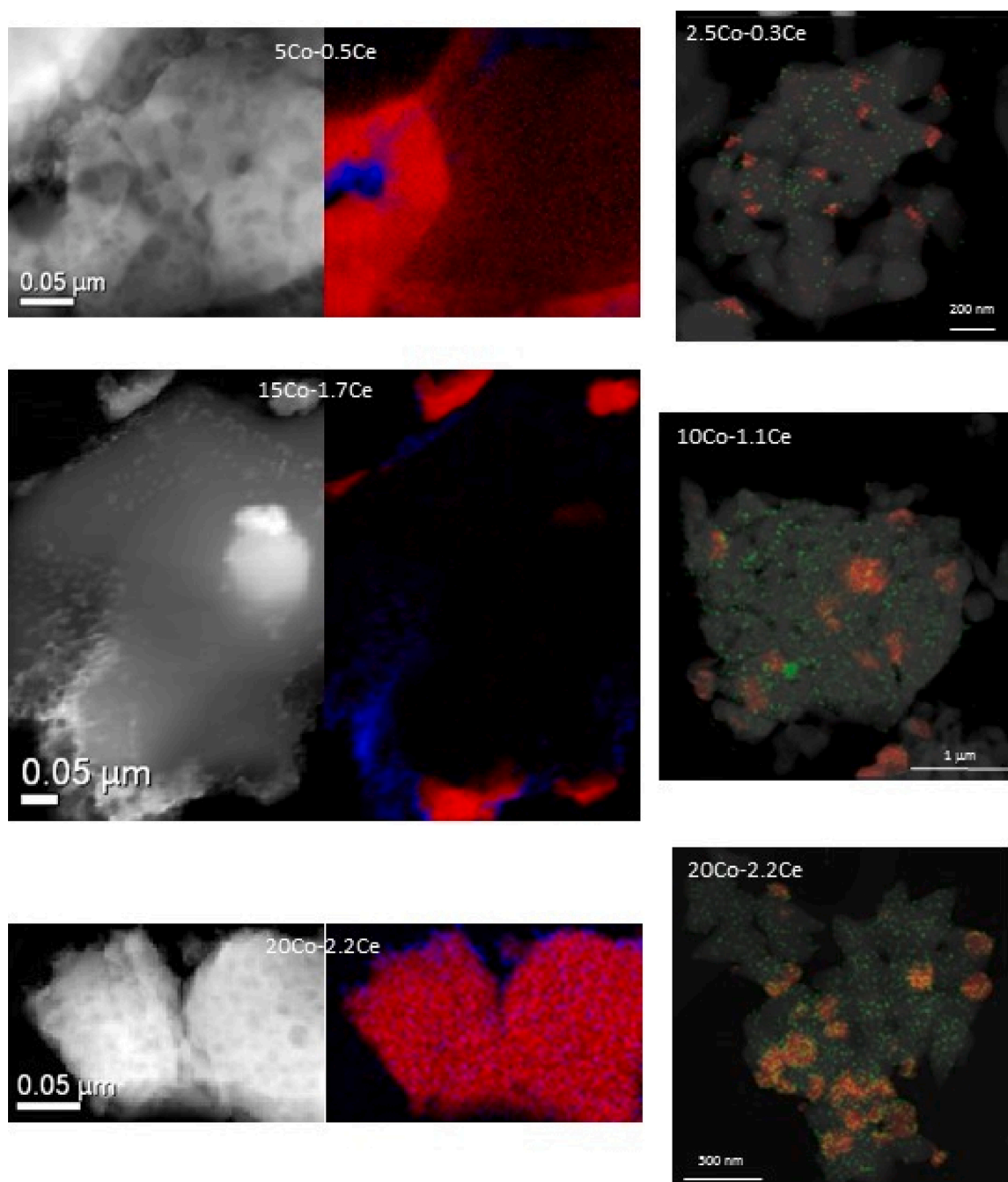
Fig. 9. STEM-HAADF images and EDX and EELS maps of selected Co-Ce catalysts with varying Co loading and a fixed Ce/Co molar ratio (0.05). (Red) cobalt and (blue) cerium for EELS maps (left); (red) cobalt and (green) cerium for EDX maps (right).

510−520 °C range, while conversion at 600 °C was between 55−61 %. The corresponding specific reaction rate was estimated under differential conditions (conversion lower than 20 %) at a constant temperature (450 °C). As reported in relation to samples with varying Ce/Co molar ratio, an attempt was made to connect the observed catalytic activity with their surface composition in terms of Co^{3+}/Co^{2+} and O_{ads}/O_{latt} molar distribution. Thus, results included in Fig. 8 revealed a strong relationship of the specific reaction rate with the relative Co^{3+} content for the Co-Ce catalysts with a Co_3O_4 loading between 2.5–10 %wt, from 0.07 mmol CH_4 g^{-1} h^{-1} (2.5Co-0.3Ce) to 0.41 mmol CH_4 g^{-1} h^{-1} (10Co-1.1Ce). Above this content, the activity was relatively similar (about 0.48 mmol CH_4 g^{-1} h^{-1}) because of their comparable Co^{3+}/Co^{2+} molar ratio close to 1.2. When normalising the kinetic results to the mass of cobalt oxide (Fig. S7, Supplementary material), the activity was

maximised for a Co_3O_4 loading of 10 %wt. In sum, judging from the results of the activity tests over both set of Co-Ce catalysts it was concluded the most active samples were the Co(10)-Ce(1.1) and Co(10)-Ce(2.1) catalysts. The best behaviour of these specific catalyst formulations was related to its favoured reducibility at lower temperatures which in turn depended on the appreciable distortion of its Co_3O_4 lattice by cerium addition. In an attempt to better reveal more marked differences in performance their efficiency was studied at varying GHSV in the 15,000–60,000 h^{-1} range (equivalent to a WHSV in the 200−800 ml g^{-1} h^{-1} range). Results included in Fig. S8 (Supplementary material) correspond to the averaged conversion at 600 °C for 4 h in steps of 3,000 h^{-1}. In addition to the expected gradual decrease in conversion at lower residence times, the better performance of the Co(10)-Ce(1.1) sample was more clearly evidenced under more demanding operating

conditions. Interestingly, upon returning to the baseline GHSV (15,000 h^{-1}) and after a total accumulated time interval of 60 h at 600 °C, the conversion recovered to the same initial level, thereby suggesting a reasonably good thermal stability of both samples.

The apparent activation energy values were in the 71−72 kJ mol^{-1} range over the Co(10)-Ce(1.1), Co(15)-Ce(1.7) and Co(20)-Ce(2.2) catalysts (Table 3 and Fig. S6, Supplementary material). As previously shown, this coincided with that observed for pure Co$_3$O$_4$ bulk oxides and the investigated Co(10)-Ce(2.1) and Co(10)-Ce(4.3) catalysts. In contrast, significantly higher activation energies were found over the Co-poor counterparts, namely the Co(2.5)-Ce(0.3) (93 kJ mol^{-1}) and Co (5)-Ce(0.5) (85 kJ mol^{-1}) samples. It is hypothesised that the formation of small amounts of less efficient CoAl$_2$O$_4$ could occur on the surface of these two samples where cobalt was comparatively better dispersed, thereby promoting the generation of this mixed oxide. Note that this would be in agreement with the observed relatively low Co^{3+}/Co^{2+} molar ratio (0.7–1.0) at their surface, thereby suggesting the presence of Co^{2+} species as CoAl$_2$O$_4$.

Given the presence of notable amounts of water vapour in the real exhaust gases of a natural gas engine, the light-off behaviour of the most active catalyst (Co(10)-Ce(1.1)) was also analysed under humid conditions (1%CH$_4$/10 %O$_2$/10 %H$_2$O/N$_2$) at 15,000 h^{-1}. This run was carried out with the same sample as that used in the corresponding light-off test under dry conditions. The corresponding results are included in Fig. S9, Supplementary material. It was found that water significantly inhibited the catalyst efficiency owing to water adsorption. The drop in conversion was somewhat more appreciable with increasing temperatures, from 17, 38 and 58 % at 500, 550, and 600 °C under dry conditions to 11, 29 and 40 %, respectively, under humid conditions. A subsequent light-off under dry conditions (not shown) evidenced that this did not preliminary result in an apparently marked catalyst deactivation. Even so, the thermal and hydrothermal stability of this sample was studied over a relatively prolonged period of operation under both dry and humid conditions. The dry (1% CH$_4$/10%O$_2$/N$_2$) and humid (1%CH$_4$/10%O$_2$/10%H$_2$O/N$_2$) feed mixtures were alternated every 25 h over a total reaction interval of 150 h at 600 °C and 200 mL CH$_4$ g^{-1} h^{-1}. The results are summarised in Fig. 10. The catalyst exhibited a notable thermal stability, not showing any significant evidence of deactivation throughout the first 25 h of operation. A fairly constant methane conversion around 62 % was found. It is worth recalling that the sample attained 60 % conversion at 600 °C in the light-off test. However, after the admission of water into the reactor during additional 25 h, conversion dropped to a stable value of 40 % due to water adsorption on the surface. Interestingly, when water was subsequently cut off, the
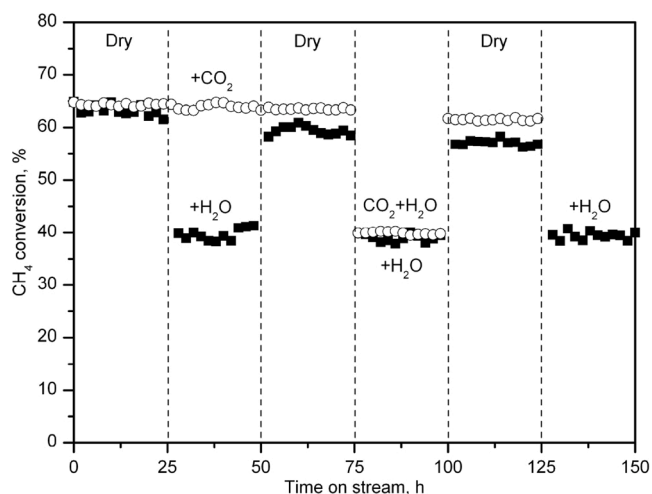
methane conversion was almost fully recovered, thus being reached the same conversion as observed under dry conditions (59 %). Thus, it was evidenced that this temporary inhibiting effect of water did not lead to a significant irreversible deactivation of the sample, as opposed to what was reported for cobalt catalysts supported over γ-Al$_2$O$_3$ [20,22,54]. No significant changes in performance were observed during the two subsequent dry/humid operation cycles. It was then concluded that the 10Co-1.1Ce exhibited a reasonably good thermal and hydrothermal stability under cycled dry/humid conditions. Additionally, attention was paid to examining the effect of the presence of carbon dioxide in the feedstream on the catalytic behaviour. Thus, the evolution of conversion at 600 °C was analysed when the composition was alternated following this sequence: 1% CH$_4$/10%O$_2$/N$_2$, 1%CH$_4$/10CO$_2$%/10%O$_2$/N$_2$, 1%CH$_4$/10%O$_2$/N$_2$, 1% CH$_4$/10H$_2$O/10CO$_2$%10%O$_2$/N$_2$ and 1%CH$_4$/10%O$_2$/N$_2$. For each composition, a reaction time interval of 25 h was analysed, with an accumulated time on stream of 125 h (Fig. 10). Interestingly, it was found that the presence of carbon dioxide had no visible negative impact on conversion, even when combined with the presence of water vapour.

In order to explain the observed notable influence of water vapour during the stability tests, the used samples were characterised by H$_2$-TPR and XRD. Hence, the H$_2$-TPR (Fig. S10, Supplementary material) clearly revealed a loss of redox properties in the form of a shift of 40−45 °C in the reduction peak temperature, although the overall H$_2$ uptake of both samples was similar to that of the fresh counterpart. In this sense, XRD analysis suggested that this lower reducibility could be due to a significant increase in the Co$_3$O$_4$ crystallite size (43−46 nm) with respect to the fresh counterpart (35 nm). It must be noted that these effects were comparable for the two stability tests, which led to the conclusion that they were essentially caused by the exposure of the catalyst to water vapour, with the addition of CO$_2$ not having any remarkable added effect.

Finally, some comparative remarks on stability under humid conditions will be made with respect to highly active palladium catalysts. Certainly, the performance of these catalysts is significantly affected by water vapour. Available works in the literature describe two deactivation mechanisms, namely a reversible, physical inhibiting effect due to competition of water molecules for active sites, and an irreversible deactivation process, which involves a structural change to form an inactive Pd phase [55]. In this sense, a reversible deactivating effect was observed over 1%Pd/Al$_2$O$_3$ and 1%Pd/SnO$_2$ samples in the presence of water vapour (5–10 %) at 48, 000 h^{-1} [56], since the initial conversion levels were fully recovered once water admission to the reactor was cut off. Analogous results were reported by Gélin et al. [57] over a 2.2 %Pd/Al$_2$O$_3$ catalyst operating under humid conditions (10 %H$_2$O) at 20,000 h^{-1}. It is worth pointing out that in both cases the time span in the presence of water was relatively short (20 h) and the reaction temperature was lower than 425 °C. However, when a noble metal catalyst was submitted to more severe hydrothermal conditions (10 %H$_2$O/650 °C/20 h), Abbasi et al. [58] found that a cordierite-supported Pt-Pd (Pt-Pd in a 4:1 ratio) bimetallic catalyst did not completely recover its initial activity. These results, along with the findings of this work, suggest that notable efforts should be made to improve the specific activity of the selected catalyst for lean methane oxidation since a significant reduction in operating temperature would also surely limit the extent of the negative impact of the unavoidable presence of water in the feedstream.

4. Conclusions

This work is focused on the analysis of the viability of Ce-modified Co$_3$O$_4$ catalysts supported on alpha alumina for the oxidation of trace amounts of methane present in the exhaust gases of natural gas engines. Attention was initially paid to examining the influence of the Ce/Co molar ratio (between 0 and 0.2) for a given Co$_3$O$_4$ loading of 10 %wt. It is worth noting that the use of alpha alumina instead of gamma alumina was suitable for preserving the chemical nature of deposited cobalt species as Co$_3$O$_4$ since the formation of undesired cobalt aluminate was greatly inhibited due to high chemical stability of this alumina

Fig. 10. Evolution of methane conversion with time on stream over the 10Co-1.1Ce catalyst under dry/humid conditions or dry/CO$_2$/CO$_2$+H$_2$O conditions at 200 mL CH$_4$ g^{-1} h^{-1} and 600 °C.

polymorph. On the other hand, it was observed that insertion of Ce into the spinel lattice was favoured for low Ce/Co molar ratios as evidenced by a relatively higher cerium dispersion, the enlargement of the cell parameter and the higher FWHM of the main Raman mode. At the same time, increased Co^{3+}/Co^{2+} molar ratios were found, which in turn resulted in a higher abundance of oxygen lattice species. As a result, Co-Ce catalysts with improved redox properties with respect to the base Ce-free cobalt counterpart were obtained as revealed by the lower onset reduction temperatures and higher H_2 uptake at low temperatures. On the other hand, the extent of the observed changes in the structure of the spinel lattice and surface chemical composition did not increase with high Ce/Co molar ratios. Thus, the behaviour of the samples with the highest Ce/Co molar ratios (0.1 and 0.2) was not substantially promoted due to partial segregation of excess cerium as agglomerated CeO_2. A Ce/Co molar ratio of 0.05 was thus fixed as the optimal composition.

The effect of the Co_3O_4 loading (2.5−20%wt.) while maintaining this Ce/Co molar ratio was examined as well. The extent of lattice distortion of the cobalt spinel by Ce insertion was similar for all synthesised samples regardless of the Co content. However, the Co_3O_4 crystallites of the samples with a 2.5−5 %wt. loading were smaller and highly stable with a poorer redox behaviour. These samples were characterised by a higher presence of Co^{2+} species, which could suggest the existence of cobalt aluminate on the surface. In contrast, sizeable crystallites in the catalysts with a higher Co loading revealed a superior intrinsic activity, with a marginal improvement over the samples with a 15−20%wt. Co_3O_4 content. From the analysis of the apparent activation energy of the ten investigated Co-Ce catalysts, the formation of trace amounts of cobalt aluminate over the samples with low Co and/or Ce loadings could be deduced. These samples showed significantly higher apparent activation energies (79−93 kJ mol^{-1}) in comparison with those typically expected for a pure Co_3O_4 catalytic phase (71−72 kJ mol^{-1}), as seen for the 10Co-1.1Ce, 10Co-2.1Ce, 10Co-Ce4.3, 15Co-1.7Ce and 20Co-2.2Ce catalysts. The presence of this less active $CoAl_2O_4$ oxide on the surface of these samples was coherent with a low Co^{3+}/Co^{2+} molar ratio on the surface. The selected optimal catalyst formulation for lean methane oxidation was 10Co-1.1Ce, with a Ce/Co molar ratio of 0.05. This sample exhibited a notable thermal stability under dry conditions. The inhibiting effect of water was found to be completely reversible, and no inhibitinf effect by CO_2 was found.

CRediT authorship contribution statement

Andoni Choya: Investigation, Writing - original draft. **Sylwia Gudyka:** Investigation. **Beatriz de Rivas:** Methodology, Validation. **Jose Ignacio Gutiérrez-Ortiz:** Methodology, Formal analysis. **Andrzej Kotarba:** Methodology, Conceptualization. **Rubén López-Fonseca:** Conceptualization, Writing - review & editing, Supervision.

Declaration of Competing Interest

The authors declare that they have no known competing financial interests or personal relationships that could have appeared to influence the work reported in this paper.

Acknowledgements

Appendix A. Supplementary data

Supplementary material related to this article can be found, in the online version, at doi:https://doi.org/10.1016/j.apcata.2021.118105.

References

[1] C. Park, S. Lee, G. Lim, Y. Choi, C. Kim, Fuel 123 (2014) 101–106, https://doi.org/10.1016/j.fuel.2014.01.041.
[2] M. Hussain, F.A. Deorsola, N. Russo, D. Fino, R. Pirone, Fuel 149 (2015) 2–7, https://doi.org/10.1016/j.fuel.2014.12.024.
[3] X. Jiang, D. Mira, D.L. Cluff, Prog. Energy Combust. Sci. 66 (2018) 176–199, https://doi.org/10.1016/j.pecs.2016.06.002.
[4] G. Ercolino, P. Stelmachowski, G. Grzybek, A. Kotarba, S. Specchia, Appl. Catal. B Environ. 206 (2017) 712–725, https://doi.org/10.1016/j.apcatb.2017.01.055.
[5] L. He, Y. Fan, J. Bellettre, J. Yue, L. Luo, Renew. Sustain. Energy Rev. 119 (2020), 109589, https://doi.org/10.1016/j.rser.2019.109589.
[6] M. Monai, T. Montini, R.J. Gorte, P. Fornasiero, Eur. J. Inorg. Chem. 25 (2018) 2884–2893, https://doi.org/10.1002/ejic.201800326.
[7] P. Velin, M. Ek, M. Skoglundh, A. Schaefer, A. Raj, D. Thompsett, G. Smedler, P.-A. Carlsson, J. Phys. Chem. C 123 (2019) 25724–25737, https://doi.org/10.1021/acs.jpcc.9b07606.
[8] H. Nassiri, R.E. Hayes, N. Semagina, Chem. Eng. Sci. 186 (2018) 44–51, https://doi.org/10.1016/j.ces.2018.04.028.
[9] M. Monai, M. Melchionna, P. Fornasiero, Adv. Catal. 63 (2018) 1–73, https://doi.org/10.1016/bs.acat.2018.10.001.
[10] L.F. Liotta, H. Wu, G. Pantaleo, A.M. Venezia, Catal. Sci. Technol. 3 (2013) 3085–3102, https://doi.org/10.1039/C3CY00193H.
[11] W. Tang, J. Weng, X. Lu, L. Wen, A. Suburamanian, C.-Y. Nam, P.-X. Gao, Appl. Catal. B Environ. 256 (2019), 117859, https://doi.org/10.1016/j.apcatb.2020.119566.
[12] W. Hu, J. Lan, Y. Guo, X.-M. Cao, P. Hu, ACS Catal. 6 (2016) 5508–5519, https://doi.org/10.1021/acscatal.6b01080.
[13] Z. Pu, H. Zhou, Y. Zheng, W. Huang, X. Li, Appl. Surf. Sci. 410 (2017) 14–21, https://doi.org/10.1016/j.apsusc.2017.05.231.
[14] Y. Guo, M. Wen, G. Li, T. An, Appl. Catal. B Environ. 281 (2021) 119447, https://doi.org/10.1016/j.apcatb.2020.119447.
[15] W. Liu, R. Liu, H. Zhang, Q. Jin, Z. Song, X. Zhang, Appl. Catal. A Gen. 597 (2020), 117539, https://doi.org/10.1016/j.apcata.2020.117539.
[16] S. Akram, Z. Wang, L. Chen, Q. Wang, G. Shen, N. Han, Y. Chen, G. Ge, Catal. Commun. 73 (2016) 123–127, https://doi.org/10.1016/j.catcom.2015.10.024.
[17] B. de Rivas, R. López-Fonseca, C. Jiménez-González, J.I. Gutiérrez-Ortiz, J. Catal. 281 (2011) 88–97, https://doi.org/10.1016/j.jcat.2011.04.005.
[18] B. Cui, L. Zhou, K. Li, Y.-Q. Liu, D. Wang, Y. Ye, S. Li, Appl. Catal. B Environ. 267 (2020), 118670, https://doi.org/10.1016/j.apcatb.2020.118670.
[19] Q. Wang, Y. Peng, J. Fu, G.Z. Kyzas, S.M.R. Billah, S. An, Appl. Catal. B Environ. 168–169 (2015) 42–50, https://doi.org/10.1016/j.apcatb.2014.12.016.
[20] A. Choya, B. de Rivas, J.R. González-Velasco, J.I. Gutiérrez-Ortiz, R. López-Fonseca, Appl. Catal. A Gen. 582 (2019), 117099, https://doi.org/10.1016/j.apcata.2019.05.033.
[21] J. González-Prior, R. López-Fonseca, J.I. Gutiérrez-Ortiz, B. de Rivas, Appl. Catal. B Environ. 222 (2018) 9–17, https://doi.org/10.1016/j.apcatb.2017.09.050.
[22] A. Choya, B. de Rivas, J.R. González-Velasco, J.I. Gutiérrez-Ortiz, R. López-Fonseca, Appl. Catal. A Gen. 591 (2020), 117381, https://doi.org/10.1016/j.apcata.2019.117381.
[23] A. Choya, B. de Rivas, J.R. González-Velasco, J.I. Gutiérrez-Ortiz, R. López-Fonseca, Catalysts 10 (2020) 757, https://doi.org/10.3390/catal10070757.
[24] B.C. Enger, Å.-L. Fossan, Ø. Borg, E. Rytter, A. Holmen, J. Catal. 284 (2011) 9–22, https://doi.org/10.1016/j.jcat.2011.08.008.
[25] C. Hernández Mejía, T.W. van Deelen, K.P. de Jong, Nat. Commun. 9 (2018) 4459, https://doi.org/10.1038/s41467-018-06903-w.
[26] B. Solsona, T.E. Davies, T. García, I. Vázquez, A. Dejoz, S.H. Taylor, Appl. Catal. B Environ. 84 (2008) 176–184, https://doi.org/10.1016/j.apcatb.2008.03.021.
[27] G. Grzybek, S. Wójcik, K. Ciura, J. Grybos, P. Indyka, M. Oszajca, P. Stelmachowski, S. Witkowski, M. Inger, M. Wilk, A. Kotarba, Z. Sojka, Appl. Catal. B Environ. 210 (2017) 34–44, https://doi.org/10.1016/j.apcatb.2017.03.053.
[28] G. Grzybek, M. Greluk, P. Indyka, K. Góra-Marek, P. Legutko, G. Slowik, S. Turczyniak-Surdack, M. Rotko, Z. Sojka, A. Kotarba, Int. J. Hydrogen Energy 45 (2020) 22658–22673, https://doi.org/10.1016/j.ijhydene.2020.06.037.
[29] S. Tang, J. Lin, K.L. Tan, Catal. Lett. 59 (1999) 129–135, https://doi.org/10.1023/A:1019001428159.
[30] F.F. Tao, J.J. Shan, L. Nguyen, Z. Wang, S. Zhang, L. Zhang, Z. Wu, W. Huang, S. Zeng, P. Hu, Nat. Commun. 6 (2015) 7798, https://doi.org/10.1038/ncomms8798.
[31] A. Choya, B. de Rivas, J.R. González-Velasco, J.I. Gutiérrez-Ortiz, R. López-Fonseca, Appl. Catal. B Environ. 237 (2018) 844–854, https://doi.org/10.1016/j.apcatb.2018.06.050.
[32] Eurokin, 2018 (Accessed 28 September 2020), http://eurokin.org/.
[33] X. Zhang, M. Zhao, Z. Song, H. Zhao, W. Liu, J. Zhao, Z. Ma, Y. Xing, New J. Chem. 43 (2019) 10868–10877, https://doi.org/10.1039/C9NJ01783F.
[34] V. D'Ippolito, G.B. Andreozzi, D. Bersani, P.P. Lottici, J. Raman Spectrosc. 46 (2015) 1255–1264, https://doi.org/10.1002/jrs.4764.

[35] C. Zhang, Y. Wang, G. Li, L. Chen, Q. Zhang, D. Wang, X. Li, Z. Wang, Appl. Surf. Sci. 532 (2020), 147320, https://doi.org/10.1016/j.apsusc.2020.147320.

[36] J. Yang, H. Liu, W.N. Martens, R.L. Frost, J. Phys. Chem. C 114 (2010) 111–119, https://doi.org/10.1021/jp911011g.

[37] P.J. Jodłowski, R.J. Jędrzejczyk, A. Rogulsk, A. Wach, P. Kuśtrowski, M. Sitarz, T. Łojewski, A. Kołodziej, J. Łojewsk, Spectrochim. Acta A Mol. Biomol. Spectrosc. 131 (2014) 696–701, https://doi.org/10.1016/j.saa.2014.05.027.

[38] J. Dupin, D. Gonbeau, P. Vinatier, A. Levasseur, Phys. Chem. Chem. Phys. 2 (2000) 1319–1324, https://doi.org/10.1039/A908800H.

[39] K. Zeng, X. Li, C. Wang, Z. Wang, P. Guo, J. Yu, C. Zhang, X.S. Zhao, J. Colloid Interfaces Sci. 572 (2020) 281–296, https://doi.org/10.1016/j.jcis.2020.03.093.

[40] J. Rosen, G.S. Hutchings, F. Jiao, J. Am. Chem. Soc. 135 (2013) 4516–4521, https://doi.org/10.1021/ja400555q.

[41] F. Zasada, J. Janas, W. Piskorz, M. Gorczynska, Z. Sojka, ACS Catal. 7 (2017) 2853–2867, https://doi.org/10.1021/acscatal.6b03139.

[42] J. Chen, C. Li, S. Li, P. Lu, L. Gao, X. Du, Y. Yi, Chem. Eng. J. 338 (2018) 358–368, https://doi.org/10.1016/j.cej.2018.01.043.

[43] L.F. Liotta, G. Di Carlo, G. Pantaleo, A.M. Venezia, G. Deganello, Appl. Catal. B Environ. 66 (2006) 217–227, https://doi.org/10.1016/j.apcatb.2006.03.018.

[44] H. Sohn, G. Celik, S. Gunduz, D. Dogu, S. Zhang, J. Shan, F.F. Tao, U.S. Ozkan, Catal. Lett. 147 (2017) 2863–2876, https://doi.org/10.1007/s10562-017-2176-4.

[45] J. González-Prior, R. López-Fonseca, J.I. Gutiérrez-Ortiz, B. de Rivas, Appl. Catal. B Environ. 199 (2016) 384–393, https://doi.org/10.1016/j.apcatb.2016.06.046.

[46] G. Grzybek, P. Stelmachowski, S. Gudyka, P. Indyka, Z. Sojka, N. Guillen-Hurtado, V. Rico-Pérez, A. Bueno-López, A. Kotarba, Appl. Catal. B Environ. 180 (2016) 622–629, https://doi.org/10.1016/j.apcatb.2015.07.027.

[47] J. Wang, A. Yoshida, P. Wang, T. Yu, Z. Wang, X. Hao, A. Abudula, G. Guan, Appl. Catal. B Environ. 271 (2020), 118941, https://doi.org/10.1016/j.apcatb.2020.118941.

[48] J.R. Paredes, E. Díaz, F.V. Díez, S. Ordóñez, Energy Fuels 23 (2009) 86–93, https://doi.org/10.1021/ef800704e.

[49] W. Barrett, S. Nasr, J. Shen, Y. Hu, R.E. Hayes, R.W.J. Scott, N. Semagina, Catal. Sci. Technol. 10 (2020) 4229–4236, https://doi.org/10.1039/D0CY00465K.

[50] N. Bahlawane, Appl. Catal. B Environ. 67 (2006) 168–176, https://doi.org/10.1016/j.apcatb.2006.03.024.

[51] P. Stefanov, S. Todorova, A. Naydenov, B. Tzaneva, H. Kolev, G. Atanasova, D. Stoyanova, Y. Karakirova, K. Aleksieva, Chem. Eng. J. 266 (2015) 329–338, https://doi.org/10.1016/j.cej.2014.12.099.

[52] X. Fan, L. Li, F. Jing, J. Li, W. Chu, Appl. Catal. B Environ. 271 (2020), 118941, https://doi.org/10.1016/j.apcatb.2020.118941.

[53] S. Gudyka, G. Grzybek, J. Grybos, P. Indyka, B. Leszczynski, A. Kotarba, Z. Sojka, Appl. Catal. B Environ. 201 (2017) 339–347, https://doi.org/10.1016/j.apcatb.2017.03.053.

[54] A. Choya, B. de Rivas, J.R. González-Velasco, J.I. Gutiérrez-Ortiz, R. López-Fonseca, Appl. Catal. B Environ. 284 (2021), 119712, https://doi.org/10.1016/j.apcatb.2020.119712.

[55] O. Mihai, G. Smedler, U. Nylén, M. Olofsson, L. Olsson, Catal. Sci. Technol. 7 (2017) 3084, https://doi.org/10.1039/C6CY02329K.

[56] R. Kikuchi, S. Maeda, K. Sasaki, S. Wennerström, K. Eguchi, Appl. Catal. A Gen. 232 (2002) 23–28, https://doi.org/10.1016/S0926-860X(02)00096-0.

[57] P. Gélin, L. Urfels, M. Primet, E. Tena, Catal. Today 83 (2003) 45–57, https://doi.org/10.1016/S0920-5861(03)00215-3.

[58] R. Abbasi, L. Wu, S.E. Wanke, R.E. Hayes, Chem. Eng. Res. Des. 90 (2012) 1930–1942, https://doi.org/10.1016/j.cherd.2012.03.003.